Extreme poleward expanding super plasma bubbles triggered by Tonga volcano eruption during the recovery phase of geomagnetic storm

P. K. Rajesh[1], Charles C. H. Lin[1], Jia-Ting Lin[1], Chi-Yen Lin[2], Jann-Yenq Liu[2], Tomoko Matsuo[3], Cheng-Yung Huang[2], Min-Yang Chou[4], Jia Yue[4], Michi Nishioka[5], Hidekatsu Jin[5], Jong-Min Choi[1], Shih-Ping Chen[1], Marty Chou[1], and Ho-Fang Tsai[2]

[1]National Cheng Kung University
[2]National Central University
[3]Ann and H.J. Smead Department of Aerospace Engineering Sciences, University of Colorado Boulder
[4]Goddard Space Flight Center
[5]National Institute of Information and Communications Technology

November 26, 2022

Abstract

The Tonga volcano eruption of 15 January 2022 unleashed a variety of atmospheric perturbations, coinciding with the recovery phase of a geomagnetic storm. The ensuing thermospheric variations created rare display of extreme poleward-expanding conjugate plasma bubbles seen in the rate of total electron content index (ROTI) over 100-150°E. This is associated with fluctuations in FORMOSAT-7/COSMIC-2 (F7/C2) ion-density measurements and spread-F signatures in ionograms, reaching ˜40°N geographic latitude. This was preceded by an unusually strong pre-reversal enhancement (PRE) in the global ionospheric specification (GIS) electron density profiles derived from F7/C2 observations. The GIS further revealed a decrease of equatorial ionization anomaly (EIA) crest density due to the storm impact. A sharp decrease of E-region conductivity by volcano-induced waves, combined with enhanced F-region wind over EIA with less ion-drag apparently intensified the PRE. The strong PRE and seed perturbations from the volcano-induced waves likely further triggered super plasma bubble activity.

Hosted file

essoar.10511527.1.docx available at https://authorea.com/users/555109/articles/605888-extreme-poleward-expanding-super-plasma-bubbles-triggered-by-tonga-volcano-eruption-during-the-recovery-phase-of-geomagnetic-storm

Extreme poleward expanding super plasma bubbles triggered by Tonga volcano eruption during the recovery phase of geomagnetic storm

P. K. Rajesh[1], C. H. Charles Lin[1], J. T. Lin[1], C. Y. Lin[2,3], J. Y. Liu[2,3], T. Matsuo[4], C. Y. Huang[5], M. Y. Chou[6,7], J. Yue[6,7], M. Nishioka[8], H., Jin[8], J. M. Choi[1], S. P. Chen[1], Marty Chou[1], and H. F. Tsai[1]

[1] Department of Earth Sciences, National Cheng Kung University, Tainan, Taiwan

[2] Center for Astronautical Physics and Engineering, National Central University, Taoyuan, Taiwan

[3] Department of Space Science and Engineer, National Central University, Taoyuan, Taiwan

[4] Ann and H.J. Smead Department of Aerospace Engineering Sciences, University of Colorado Boulder, CO, USA

[5] National Space Organization, Hsinchu, Taiwan

[6] NASA Goddard Space Flight Center, Community Coordinated Modeling Center, Greenbelt,

MD, USA

[7] Physics Department, Catholic University of America, Washington, DC, USA

[8] The National Institute of Information and Communications Technology, Tokyo, Japan

Key points:

1. Tonga volcano eruption during a magnetic storm recovery phase triggered extreme equatorial plasma bubbles appearing even beyond Tokyo.
2. The volcano-induced wave perturbations and unusually strong pre-reversal enhancement (PRE) result in the rare development of plasma bubbles.
3. Reduced E-region conductivity by the wave propagation and enhanced F-region wind by negative storm at the equatorial anomaly intensify PRE.

Abstract

The Tonga volcano eruption of 15 January 2022 unleashed a variety of atmospheric perturbations, coinciding with the recovery phase of a geomagnetic storm. The ensuing thermospheric variations created rare display of extreme poleward-expanding conjugate plasma bubbles seen in the rate of total electron content index (ROTI) over 100-150°E. This is associated with fluctuations in FORMOSAT-7/COSMIC-2 (F7/C2) ion-density measurements and spread-F signatures in ionograms, reaching ~40°N geographic latitude. This was preceded by an unusually strong pre-reversal enhancement (PRE) in the global ionospheric specification (GIS) electron density profiles derived from F7/C2 observations. The GIS further revealed a decrease of equatorial ionization anomaly (EIA) crest density due to the storm impact. A sharp decrease of E-region conductivity by volcano-induced waves, combined with enhanced F-region wind over EIA with less ion-drag apparently intensified the PRE. The strong PRE and seed perturbations from the volcano-induced waves likely further triggered super plasma bubble activity.

Plain Language Summary:

Rare things could happen when the centennial volcanic eruption occurred at the late stages of a magnetic storm driven by solar wind disturbances. The volcanic eruption drove atmosphere waves at the lower altitude in the ionosphere and the storm effect enhanced eastward wind at higher altitudes. The combined effect led to an unusual and substantial uplift of the post-sunset ionosphere, known as pre-reversal enhancement (PRE). Th large layer uplift destabilized the bottomside ionosphere, leading to vigorous bubble-like plasma irregularities, or plasma bubbles extending to middle latitudes, which are very rarely seen in January when the solar activity is low. This is the first time such super plasma bubbles are produced by the joint influence of geomagnetic and atmospheric forcings from above and below.

1. Introduction

Equatorial plasma bubbles (EPBs) are the irregularities in the post-sunset equatorial/low-latitude ionosphere, manifesting as spread-F in ionograms (Berkner and Wells, 1934), scintillations in radio signals (Whitney and Malik, 1968), bite-outs in ion density measurements (Hanson and Sanatani, 1973), plume structures in radar maps (Woodman and LaHoz, 1976), and intensity depletions in airglow images (Weber et al., 1978). EPBs are initiated by Rayleigh-Taylor instability (Dungey, 1956) operating in presence of seed perturbation in the post-sunset bottom-side F-region where vertical plasma density gradient is anti-parallel to gravity, with favorable background conditions of sharper plasma density gradients, smaller ion-neutral collisions, and stronger vertical plasma drifts (Sultan, 1996). The history and progress in the understanding of EPBs as well as diagnostic methods have been reported in several review articles (Glover, 1960; Farley et al., 1970; Ossakow, 1981; Hysell, 2000; Yokoyama, 2017).

Notwithstanding extensive numerous studies since the first known report, the generation and occurrence of EPBs are still one of the most intriguing topics in ionospheric research. This continuing interest stems from the unpredictable nature of the occurrence of bubbles owing to various factors that control and contribute to their generation and growth. The uncertainty arises from the variations of initial seed perturbation (Kelley et al., 1981; Abdu et al., 2009; Wu et al., 2015), neutral wind (Mendillo et al., 1992; 2001; Valladares et al., 2002), electric field (Abdu et al., 1981; Sekar and Kelley, 1998, Huang and Hairston, 2015), and bottom-side structures (Tsunoda et al., 2010a; Chou et al., 2020). Along with the inherent day-to-day variability of these parameters, external factors could also influence the occurrence of EPBs.

Apart from the gravity wave induced seed perturbations, major external factors that controls the occurrence of EPBs are geomagnetic storms, either amplifying or suppressing the bubble generation (Wright et al., 1956; Rastogi et al., 1981; Aarons, 1991; Whalen, 2002; Rajesh et al., 2017a; 2017b; Sripathi et al., 2019). The past studies mostly reported the impact of prompt penetration and/or disturbance dynamo electric field in either aiding or suppressing the pre-reversal enhancement (PRE), leading to the generation/inhibition of bubbles, and occasionally in the post-midnight irregularities. In a few cases, strong prompt penetration electric fields are shown to generate super plasma bubbles, which reach much higher latitudes (Ma and Maruyama, 2006; Cherniak and Zakharenkova, 2016; Aa et al., 2018).

This paper investigates a similar super plasma bubble activity that occurred after the Tonga volcano eruption of 15 January 2022. This mammoth eruption generated unprecedented wave perturbations in the atmosphere and ionosphere (Lin et al., 2022; Themens et al., 2022; Wright et al., 2022). One of the extraordinary ionospheric responses was the coupling of the perturbed fields along geomagnetic field lines to conjugate hemispheres, triggering ionosphere variations much earlier than anticipated (Lin et al., 2022). Furthermore, the eruption occurred in the recovery phase of a moderate geomagnetic storm (for the storm description, see Lin et al., 2022). This unique coincidence of the perturbations due to the volcano eruption with geomagnetic storm produced a rare display of plasma irregularities after sunset over East Asian longitudes (100-160°), reaching magnetic latitudes (MagLat) as far as ~35°. Such super plasma bubbles triggered by the perturbations from a volcano eruption are unheard of, offering the opportunity to examine the impacts of complex electrodynamic variations concurrently induced by the eruption and storm in the post-sunset period. The paper discusses the possible factors contributing to the generation of the observed irregularities.

1. Data Analysis

This study uses the total electron content (TEC) measurements from ground-based global navigation satellite system (GNSS) receivers, ionograms collected over Japan and Australia, in-situ and radio occultation (RO) measurements by FORMOSAT-7/COSMIC-2 (F7/C2) satellites, and the Global Ionospheric Specification (GIS) electron density profiles constructed by assimilating F7/C2 RO and GNSS slant TECs (Lin et al., 2017). The GIS has been validated with ionosonde measurements (C. Y. Lin et al., 2020), and applied to study day-to-day ionosphere variability (Rajesh et al., 2021a), ionospheric response to geomagnetic storms (Rajesh et al., 2021b), and sudden stratospheric warmings (J. T. Lin et al. 2019; 2020).

The GNSS networks in New Zealand, Australia, Japan and Taiwan are used to derive vertical TEC. The occurrence and evolution of EPBs are then inferred by calculating the rate of TEC index (ROTI) with an averaging period of 5-minutes (Pi et al., 1997). To distinguish the ROTI by volcanogenic TIDs, the TEC variations are also examined by applying a 10–60-minute bandpass filter (e.g., Lin et al., 2022). The ionosonde stations at Kokubunji (Japan) and Townsville (Australia) allow the examination of the onset and development of spread-F at either side of the magnetic equator. In-situ ion density measurements by F7/C2 ion velocity meter (IVM) detect plasma irregularities along satellite track. The GIS is constructed by using TECs from about 7000 GNSS stations worldwide. The average of three previous quiet-days (11-13 January) GIS is used as reference to quantify the variations.

1. **Results**

Figure 1 displays the absolute TEC, ROTI, and filtered TEC over the East Asian longitudes at the selected time intervals of ~0941 and ~1123 UT. A stripe of very low TEC, marked by red arrow, is seen over Australia over ~145°E and 10-20°S, though no such pattern exists over Japan possibly due to the low background. While such a depletion resembling EPB is rare to be spotted in background TEC, the most striking features are the strong ROTI values coinciding with the depletion, confirming intense plasma irregularities over this region. These ROTI enhancements show remarkable conjugate pattern, appearing over both Australia and Japan, exhibiting reverse C-shape. The filtered TEC maps in Figure 1 also show concentric TIDs generated by the volcano-induced Lamb waves. Based on the locations and orientation, the strong ROTI regions are apparently unrelated to these TIDs.

The time evolution of enhanced ROTI regions is further examined in Figure 2, portraying the poleward expansion of irregularities in succession in the western longitudes with the sunset. The distribution of the irregularities exhibits westward tilt typical of EPBs, reaching maximum poleward latitudes of ~35°N MagLat. The magnetic conjugate nature of the poleward expanding ROTI regions is evident over the eastern longitudes with more data coverage, with the strong ROTI regions over Japan at 0945 UT and the corresponding regions over Australia exhibiting identical westward tilt at the poleward ends. This conjugate alignment is evident in the subsequent frames, also for the second strong ROTI region at 1030 UT to the west of the earlier one. As time progresses, these ROTI regions expand further poleward with their locations slowly shifting eastward and, new irregularities developing to the west.

The F7/C2 IVM ion density in Figure 2 also shows perturbations when the satellites overpass the longitudes of strong ROTI under F-region sunset. At 0945 UT, the IVM scanning over 10-15° MagLat detected two consecutive plasma bubbles, where the eastern bubble aligns with the poleward conjugate structure of the strong ROTI, confirming that the ROTI values are related to vertically rising equatorial bubbles. The bubble located to the west of the one described above is also aligned with strong ROTI that was about to emerge over Japan region, indicating EPBs are still evolving. At 1000 UT, a second F7/C2 IVM also scans the same EPBs, with latter passing over latitudes just to the south of the magnetic equator, ascertaining that the strong ROTI regions are linked to the EPBs. This further offers a rare opportunity to gain multi-point perspectives of the same plasma bubbles at equatorial, low- and mid-latitude locations by combining ground-based and in-situ platforms. At 1130 UT, two such IVM scans over 120°E show irregularities near the equator and over the strong ROTI regions at low-latitudes, once again giving direct observational evidence that the strong ROTI are associated with bubbles at the equator with magnetic field-line alignment.

A movie of these observations featuring a complete time evolution of the irregularities is provided as supporting information (Movie S1), which also includes the corresponding absolute and filtered TECs. Though the concentric TIDs after the eruption yield strong ROTI, they essentially propagate westwards over Australia and north-westward over Japan (Movie S1). In contrast, the poleward expanding ROTI bands appear mostly stationary, and show an eastward moving tendency (Figure 2 and Movie S1), corroborating their EPB link.

The apex projection of ROTI in Figure 3 illustrates the extreme altitudes attained by the irregularities over the equator, offering a unique view resembling towering giant plume structures seen in JULIA radar measurements (Hysell and Burcham, 1999). Note that the irregularities here penetrate as high as ~3000 km, whereas the maximum altitudes in radar maps are usually <1000 km, demonstrating the intense nature of the EPBs triggered after the eruption. The apex projection further facilitates the estimation of vertical rise velocities of the EPBs, revealing rapidly upward drifting irregularities at speeds of 420-280 m/s till altitudes of ~1500 km and drops below 200 m/s as the bubbles rise further (Figure S1). Such large upward velocities enable the irregularities to reach extreme poleward latitudes. Strong spread-F was recorded in the ionograms over Kokubunji (28.8°N MagLat; 139.5°E) and Townsville (28.4°S MagLat.; 146.8°E) on this evening (Figure S2), independently confirming the irregularities observed in ROTI maps at such large magnetic latitudes.

To understand the background electron density distribution, GIS maps at 300 km during 0730-1030 UT are stacked together in Figure 4 (e-h), with the average of previous three quiet-days as reference (a-d), along with the difference between the two (i-l). The GIS incudes measurements taken within ± 30 minutes of the marked times. Note a sharp collapse of the southern equatorial ionization anomaly (EIA) crest over the sunlit longitudes along with strengthening of the northern crest at earlier local-time sectors compared to the reference. The crest separation is drastically reduced. The variations along the sunset terminator over the East Asian longitudes on the eruption day are even more dramatic, with the enhanced EIA crest latitudes surpassing the corresponding noon-time locations, indicating an extremely intense PRE. The beginning of the strong PRE almost coincides with the arrival of the barometric Lamb wave over the magnetic equator. Panels (e)-(h) demonstrates the collapse of the dayside EIA density structure, especially the southern crest, with an equatorward displacement of the crest latitude and the intense PRE in the evening sector.

The vertical slices at 140°E in Figure 4 (m-p) further show how intense the PRE was in this evening. At 0900 UT (~1820 LT) the F-peak altitude (hmF_2) is approximately 525 km (Figure 4n), which is ~200 km above the corresponding reference value (Figure 4m), with extremely low electron density underneath. About 1-hour later, the electron density distribution shows further strengthening of the PRE, with the hmF_2 over the magnetic equator rising above 550 km altitude (Figure 4p). The overplotted vertical electron density gradient peaks over 350-450 km altitudes, much higher than the 220 km reference height. The vertical variation of hmF_2 estimated from GIS electron density over 140°E during 0700-1000 UT yields ~40 m/s, more than thrice the reference value (Figure S3).

1. **Discussion**

The results presented here show that the phenomenal Tonga volcano eruption perturbed the post-sunset electron density distribution over the entire East Asian longitudes spanning several thousands of kilometers, producing EPBs that lasted several hours. The meridionally-extended bands of strong ROTI regions in the conjugate hemispheres after the eruption, with characteristic reverse C-shape often seen in airglow depletions, offer a unique perspective of the EPBs thus far reported by GNSS observations (Figures 1-2, Movie S1). The apex altitude projection (Figure 3) further reveals the extreme nature of the irregularities, giving the perception of giant plume structures penetrating to even 3000 km over the equator. Such wide-spread, long-lasting, and extremely upward/poleward expanding super plasma bubbles after a volcano eruption are reported for the first time, revealing the space weather consequences triggered by the seismic activities occurring far below the ground.

Though super plasma bubbles are reported during severe magnetic disturbances (Ma and Maruyama, 2006; Cherniak and Zakharenkova, 2016; Aa et al., 2018), those were during more favorable seasons or solar activity. The prevailing solstice conditions over the East Asian longitudes in the middle of January, yielding stronger inter-hemispheric winds and inclined alignment of solar terminator with magnetic meridian, least favors the generation of EPBs (Burke et al., 2004; Nishioka et al., 2008). Although irregularities could still occur with suitable seed perturbations (McClure et al., 1998; Tsunoda, 2010b), they seldom reach such higher altitudes. The generation of such super bubbles under these circumstances, as reported here, is facilitated by the extremely intense PRE that persisted for ~3-hours, which lifted the F-layer ~200 km and produced sharp plasma density gradient at altitudes of ~500 km (Figures 4 and S3). Under such background conditions, the atmospheric disturbances after the Tonga eruption could provide seed perturbations to instigate EPBs at the elevated F-region bottom-side.

However, it is unusual to observe such strong PRE of ~40 m/s (Figures 3 and

S3) in the East Asian longitudes in solstice under low solar activity. Note that E-region conductivity is crucial for the generation of PRE (Richmond and Fang, 2015a). During solstice, the finite E-region conductivity in the winter hemisphere inhibits the development of polarization electric fields by F-region dynamo. However, wave perturbations produced by the Tonga eruption (e.g., Lin et al., 2022) could reduce the E-region Pederson conductivity through ExB drifts as shown by Chou et al. (2021), supporting the development of PRE. Sharp decrease of electron density is also reported related to such seismic events (Shiagawa et al., 2013; Zettergren et al., 2017). Moreover, dynamo electric fields associated with the strong neutral wind perturbations after the Tonga eruption (Harding et al., 2022; Le et al., 2022) could further elevate the ionosphere through ExB drifts (Huba et al., 2015).

In addition, disturbance dynamo effect of the geomagnetic storm weakened the equtorial fountain (e.g., Lin et al., 2007) and yielded positive (negative) storm responses in the winter (summer) hemisphere in mid-latitude due to composition disturbances (Fuller-Rowell et al., 1996). As a result, the EIA crests on the eruption day move closer to the magnetic equator, producing sharp electron density decrease in the southern hemisphere (Figure 4). Near the terminator, the diminished EIA crest density would enable stronger F-region eastward wind due to reduced ion-drag. Richmond and Fang (2015b) demonstrated that F-region zonal winds over EIA is crucial in controlling the PRE strength. The stronger wind would mobilize ions with the flow and generate stronger PRE resulting from the vortical plasma motions over the equator in the evening ionosphere (Lee et al., 2015) to supply additional plasma.

A combination of such effects as illustrated in Figure 5 leads to the extreme evening updrift of the F-layer during the solstice period under low solar-activity, ensuring suitable background conditions for the RT instability. Under such favoring circumstances, the strong initial seed perturbations by the volcano-induced disturbances could rapidly generate very intense EPBs. According to Tsunoda (2010c), neutral wind perturbations associated with circular gravity waves are more efficient in generating a net field-line integrated polarization electric field, with the wavelength of the gravity wave of the order or larger than the distance from the source regions. Over the East Asian longitudes studied here, the arrival of barometric Lamb wave over equator coincides with the E-region sunset, or even lags (Figure 1; Movie S1). As the Lamb wave propagation could continuously trigger concentric gravity waves of wavelengths 500-1500 km (Lin et al., 2022), this would ensure sufficient polarization electric fields to provide seed perturbations. Thus, the unusually strong PRE and the ensuing sharp plasma density gradients, with the strong seed perturbations after the volcano eruption resulted in very rapid growth of the RT instability yielding the observed super plasma bubbles.

Note that EPBs usually take about 1-2 hours to appear over low-latitudes regions after onset. In the ROTI maps (Movie S1), over ~140°E, strong values that expand poleward appear around 1010 UT over 31.3°N, with apex altitude of ~1660 km. The E-region sunset over equator at this longitude was ~0917 UT, requiring the bubble ~53 minutes to reach such altitudes. Considering that EPBs are generated ~450 km, this suggests ~380 m/s vertical rise velocity for the bubbles. The EPB velocity at 145°E reveal such large values, whereas it is slower for the EPB at 140°E (Figure S1). However, the estimated bubble rise velocities are affected by the westward tilt and the eastward drift. Moreover, the initial rise velocity of the bubbles could be much larger as shown by Chou et al. (2021). Further, the TIDs that co-exist with the EPBs (Movie S1) could also contribute to the vertical rise velocity when the associated polarization electric fields are in phase with those within the bubbles. The strong westward tilt of EPBs point to such interactions (Chou et al. 2021).

1. **Conclusion**

The reduced E-region conductivity by the passage of barometric Lamb wave after the Tonga volcano eruption enable strong PRE in the solstice period, which is amplified by enhanced zonal winds over EIA due to negative geomagnetic storm response, drawing plasma upward over the equator. Under such suitable conditions, irregularities that updraft rapidly are generated by the seed perturbations by the Lamb wave driven gravity waves, producing super plasma bubbles reaching extremely poleward latitudes. The results, for the first time, show such intense EPBs by a volcanic eruption, highlighting the unprecedented space weather impacts triggered by a dramatic seismic event.

Acknowledgements

This work is partly supported by the Ministry of Science and Technology under MOST-110-2111-M-006-004 and MOST-110-2119-M-006-001 and National Space Organization under NSPO-S-110296. TM acknowledges support from NSF awards AGS 1848544. The authors acknowledge the Geological hazard information for New Zealand, Geoscience Australia, Geospatial Information Authority of Japan, Central Weather Bureau, Taiwan for managing the GNNS observations, and the Space Weather Services of the Bureau of Meteorology of Australia for ionograms.

Open Research

The GNSS TEC and GIS data used in this study are available at https://doi.org/10.6084/m9.figshare.19913590.v1. The ionograms are available at the Bureau of Meteorology, Government of Australia (https://www.sws.bom.gov.au/HF_Systems/1/3) and National Institute of Information and Communications Technology, Japan (https://wdc.nict.go.jp/ionog/js_viewer/js_01.html).

References

Aa, E., Huang, W., Liu, S., Ridley, A., Zou, S., Shi, L., et al. (2018). Midlatitude plasma bubbles over China and adjacent areas during a magnetic storm on 8 September 2017. Space Weather, 16, 321– 331. https://doi.org/10.1002/2017SW001776.

Aarons, J. (1991), The role of the ring current in the generation or inhibition of equatorial F layer irregularities during magnetic storms, Radio Sci., 26(4), 1131– 1149, doi:10.1029/91RS00473.

Abdu, M. A., Alam Kherani, E., Batista, I. S., de Paula, E. R., Fritts, D. C., and Sobral, J. H. A. (2009), Gravity wave initiation of equatorial spread F/plasma bubble irregularities based on observational data from the SpreadFEx campaign, Ann. Geophys., 27, 2607–2622, https://doi.org/10.5194/angeo-27-2607-2009.

Abdu, M. A., Bittencourt, J. A., and Batista, I. S. (1981), Magnetic declination control of the equatorial F region dynamo electric field development and spread F, J. Geophys. Res., 86(A13), 11443– 11446, doi:10.1029/JA086iA13p11443.

Berkner, L. V., and Wells, H. W. (1934), F-region ionosphere-investigations at low latitudes, Terr. Magn. Atmos. Electr., 39(3), 215– 230, doi:10.1029/TE039i003p00215.

Blanc, M., and Richmond, A. (1980), The ionospheric disturbance dynamo, J. Geophys. Res., 85(A4), 1669– 1686, doi:10.1029/JA085iA04p01669.

Burke, W. J., Gentile, L. C., Huang, C. Y., Valladares, C. E., and Su, S. Y. (2004), Longitudinal variability of equatorial plasma bubbles observed by DMSP and ROCSAT-1, J. Geophys. Res., 109, A12301, doi:10.1029/2004JA010583.

Cherniak, I., and Zakharenkova, I. (2016), First observations of super plasma bubbles in Europe, Geophys. Res. Lett., 43, 11,137– 11,145, doi:10.1002/2016GL071421.

Chou, M.-Y., C. C. H. Lin, and J. D. Huba. (2021), Modeling the disappearance of equatorial plasma bubble by nighttime medium-scale traveling ionospheric disturbances. Terr. Atmos. Ocean. Sci., 32, 217-228, doi:10.3319/TAO.2021.03.30.01.

Chou, M.-Y., Pedatella, N. M., Wu, Q., Huba, J. D., Lin, C. C. H., Schreiner, W. S., et al. (2020). Observation and simulation of the development of equatorial plasma bubbles: Post-sunset rise or upwelling growth?. Journal of Geophysical Research: Space Physics, 125, e2020JA028544. https://doi.org/10.1029/2020JA028544

Dungey, J. W. (1956), Convective diffusion in the equatorial F region, Journal of Atmospheric and Terrestrial Physics, Volume 9, Issues 5–6, Pages 304-310. https://doi.org/10.1016/0021-9169(56)90148-9.

Farley, D. T., Balsey, B. B., Woodman, R. F., and McClure, J. P. (1970), Equatorial spread F: Implications of VHF radar observations, J. Geophys. Res., 75(34), 7199– 7216, doi:10.1029/JA075i034p07199.

Glover, F. N. (1960), A survey of spread F. NBS Tech. Note 82. Boulder Laboratories, Colorado.

Harding, B. J., Wu, Y.-J. J., Alken, P., Yamazaki, Y., Triplett, C. C., Immel, T. J., et al. (2022). Impacts of the January 2022 Tonga volcanic eruption on the ionospheric dynamo: ICON-MIGHTI and Swarm observations of extreme neutral winds and currents. Geophysical Research Letters, 49, e2022GL098577. https://doi.org/10.1029/2022GL098577.

Haerendel, G., and Eccles, J. V. (1992), The role of the equatorial electrojet in the evening ionosphere, J. Geophys. Res., 97(A2), 1181– 1192, doi:10.1029/91JA02227.

Hanson, W. B., and Sanatani, S. (1973), Large Ni gradients below the equatorial F peak, J. Geophys. Res., 78(7), 1167– 1173, doi:10.1029/JA078i007p01167.

Huang, C., and Hairston, M. R. (2015), The postsunset vertical plasma drift and its effects on the generation of equatorial plasma bubbles observed by the C/NOFS satellite. J. Geophys. Res. Space Physics, 120, 2263– 2275. doi:10.1002/2014JA020735.

Huba, J. D., Drob, D. P., Wu, T.-W., and Makela, J. J. (2015), Modeling the ionospheric impact of tsunami-driven gravity waves with SAMI3: Conjugate effects, Geophys. Res. Lett., 42, 5719– 5726, doi:10.1002/2015GL064871.

Hysell, D. L. (2000), An overview and synthesis of plasma irregularities in equatorial spread F. Journal of Atmospheric and Terrestrial Physics, Volume 62, Issue 12, Pages 1037-1056. https://doi.org/10.1016/S1364-6826(00)00095-X.

Hysell, D. L., and Burcham, J. D. (1998), JULIA radar studies of equatorial spread F, J. Geophys. Res., 103(A12), 29155– 29167, doi:10.1029/98JA02655.

Fuller-Rowell, T. J., Codrescu, M. V., Rishbeth, H., Moffett, R. J., and Quegan, S. (1996), On the seasonal response of the thermosphere and ionosphere to geomagnetic storms, J. Geophys. Res., 101(A2), 2343– 2353, doi:10.1029/95JA01614.

Kelley, M. C., Larsen, M. F., LaHoz, C., and McClure, J. P. (1981), Gravity wave initiation of equatorial spread F: A case study, J. Geophys. Res., 86(A11), 9087–9100, doi:10.1029/JA086iA11p09087.

Le, G., Liu, G., Yizengaw, E., Englert, C. R. (2022), Intense Equatorial Electrojet and Counter Electrojet caused by the 15 January 2022, Earth and Space Science Open Archive, Retrieved from https://www.essoar.org/doi/abs/10.1002/essoar.10511040.2. https://doi.org/10.1002/essoar.10511040.2.

Lee, W. K., Kil, H., Kwak, Y.-S., and Paxton, L. J. (2015), Morphology of the postsunset vortex in the equatorial ionospheric plasma drift, Geophys. Res. Lett., 42, 9– 14, doi:10.1002/2014GL062019.

Lin, C. H., J. Y. Liu, H. F. Tsai, and C. Z. Cheng, (2007), Variations in the equatorial ionization anomaly peaks in the Western Pacific region during the geomagnetic storms of April 6 and July 15, 2000, *Earth Planets and Space*, 59, 5, 401-405, ISSN: 1343-8832.

Lin, C.-Y., C. C.-H. Lin, J.-Y. Liu, P. K. Rajesh, T. Matsuo, M.-Y. Chou, et al. (2020), The early results and validation of FORMOSAT-7/COSMIC-2 space weather products: Global ionospheric specification and Ne-aided Abel electron density profile, J. Geophys. Res. Space Phys., 125, e2020JA028028. https://doi.org/10.1029/2020JA028028

Lin, C. Y., T. Matsuo, J. Y. Liu, C. H. Lin, J. D. Huba, H. F. Tsai, & C. Y. Chen (2017), Data assimilation of ground- based GPS and radio occultation total electron content for global ionospheric specification, J. Geophys. Res. Space Phys., 122, 10,876–10,886. https://doi.org/10.1002/2017JA024185.

Lin, J. T., C. H. Lin, P. K. Rajesh, J. Yue, C. Y. Lin, and T. Matsuo (2020), Local-time and vertical characteristics of quasi-6-day oscillation in the ionosphere during the 2019 Antarctic Sudden Stratospheric Warming, Geophysical Research Letters, 47, e2020GL090345. https://doi.org/10.1029/2020GL090345.

Lin, J. T., Lin, C. H., Lin, C. Y., Pedatella, N. M., Rajesh, P. K., Matsuo, T., & Liu, J. Y. (2019). Revisiting the modulations of ionospheric solar and lunar migrating tides during the 2009 stratospheric sudden warming by using global ionosphere specification. Space Weather, 17, 767–777. https://doi.org/10.1029/2019SW002184.

Lin, J.-T., Rajesh, P. K., Lin, C. C. H., Chou, M.-Y., Liu, J.-Y., Yue, J., et al. (2022). Rapid conjugate appearance of the giant ionospheric Lamb wave signatures in the northern hemisphere after Hunga-Tonga volcano eruptions. Geophysical Research Letters, 49, e2022GL098222. https://doi.org/10.1029/2022GL098222.

Ma, G., and Maruyama, T. (2006), A super bubble detected by dense GPS network at east Asian longitudes, Geophys. Res. Lett., 33, L21103, doi:10.1029/2006GL027512.

McClure, J. P., Singh, S., Bamgboye, D. K., Johnson, F. S., and Kil, H. (1998), Occurrence of equatorial F region irregularities: Evidence for tropospheric seeding, J. Geophys. Res., 103(A12), 29119– 29135, doi:10.1029/98JA02749.

Mendillo, M., Baumgardner, J., Pi, X., Sultan, P. J., and Tsunoda, R. (1992), Onset conditions for equatorial spread F, J. Geophys. Res., 97(A9), 13865–13876, doi:10.1029/92JA00647.

Mendillo, M., Meriwether, J., and Biondi, M. (2001), Testing the thermospheric neutral wind suppression mechanism for day-to-day variability of equatorial spread F, J. Geophys. Res., 106(A3), 3655– 3663, doi:10.1029/2000JA000148.

Nishioka, M., Saito, A., and Tsugawa, T. (2008), Occurrence characteristics of plasma bubble derived from global ground-based GPS receiver networks, J. Geophys. Res., 113, A05301, doi:10.1029/2007JA012605.

Ossakow, S. L. (1981), Spread-F theories-a review. Journal of Atmospheric and Terrestrial Physics, Volume 43, Issues 5–6, Pages 437-452, https://doi.org/10.1016/0021-9169(81)90107-0.

Pi, X., A. J. Mannucci, U. J. Lindqwister, and C. M. Ho (1997), Monitoring of global ionospheric irregularities using the worldwide GPS network, Geophys.

Res. Lett., 24(18), 2283–2286, doi:10.1029/97GL02273.

Rajesh, P. K., C. H. Lin, C. H. Chen, W. H. Chen, J. T. Lin, M. Y. Chou, M. T. Chang, and C. F. You(2017a), Global equatorial plasma bubble growth rates using ionosphere data assimilation, *J. Geophys. Res. Space Physics*, 122, 3777–3787, doi:10.1002/2017JA023968.

Rajesh, P. K., C. H. Lin, C. H. Chen, J. T. Lin, T. Matsuo, M. Y. Chou, W. H. Chen, M. T. Chang and C. F. You (2017b), Equatorial plasma bubble generation/inhibition during 2015 St. Patrick's Day storm, *Space Weather*, 15, doi:10.1002/2017SW001641

Rajesh, P. K., C. H. Lin, J. T. Lin, C. Y. Lin, J. Yue, T. Matsuo, S. P. Chen and C. H. Chen (2021a), Day-to-day Variability of Ionosphere Electron Density During Solar Minimum Derived from FORMOSAT-7/COSMIC-2 Measurements, Terr. Atmos. Ocean. Sci., 32, 959-975, doi:10.3319/TAO.2021.08.01.01.

Rajesh, P. K., C. H. Lin, C. Y. Lin, C. H. Chen, J. Y. Liu, T. Matsuo et al. (2021b), Extreme positive ionosphere storm triggered by a minor magnetic storm in deep solar minimum revealed by FORMOSAT-7/COSMIC-2 and GNSS observations. J. Geophys. Res. Space Phys., 126, e2020JA028261. https://doi org/10.1029/2020JA028261.

Rastogi, R. G., Mullen, J. P., and MacKenzie, E. (1981), Effect of geomagnetic activity on equatorial radio VHF scintillations and spread F, J. Geophys. Res., 86(A5), 3661– 3664, doi:10.1029/JA086iA05p03661.

Richmond, A. D., Fang, T. -W., and Maute, A. (2015a), Electrodynamics of the equatorial evening ionosphere: 1. Importance of winds in different regions. J. Geophys. Res. Space Physics, 120, 2118– 2132. doi: 10.1002/2014JA020934.

Richmond, A. D., and Fang, T. -W. (2015b), Electrodynamics of the equatorial evening ionosphere: 2. Conductivity influences on convection, current, and electrodynamic energy flow. J. Geophys. Res. Space Physics, 120, 2133– 2147. doi: 10.1002/2014JA020935.

Sekar, R., and Kelley, M. C. (1998), On the combined effects of vertical shear and zonal electric field patterns on nonlinear equatorial spread F evolution, J. Geophys. Res., 103(A9), 20735– 20747, doi:10.1029/98JA01561.

Shinagawa, H., Tsugawa, T., Matsumura, M., Iyemori, T., Saito, A., Maruyama, T., Jin, H., Nishioka, M., and Otsuka, Y. (2013), Two-dimensional simulation of ionospheric variations in the vicinity of the epicenter of the Tohoku-oki earthquake on 11 March 2011, Geophys. Res. Lett., 40, 5009– 5013, doi:10.1002/2013GL057627.

Sripathi, S., Banola, S., Emperumal, K., Suneel Kumar, B., & Radicella, S. M. (2018). The role of storm time electrodynamics in suppressing the equatorial plasma bubble development in the recovery phase of a geomagnetic storm. Journal of Geophysical Research: Space Physics, 123, 2336– 2350. https://doi.org/10.1002/2017JA024956

Sultan, P. J. (1996), Linear theory and modeling of the Rayleigh-Taylor instability leading to the occurrence of equatorial spread F, J. Geophys. Res., 101(A12), 26875– 26891, doi:10.1029/96JA00682.

Themens, D. R., Watson, C., Žagar, N., Vasylkevych, S., Elvidge, S., McCaffrey, A., et al. (2022). Global propagation of ionospheric disturbances associated with the 2022 Tonga volcanic eruption. Geophysical Research Letters, 49, e2022GL098158. https://doi.org/10.1029/2022GL098158.

Tsunoda, R. T., Bubenik, D. M., Thampi, S. V., and Yamamoto, M. (2010), On large-scale wave structure and equatorial spread F without a post-sunset rise of the F layer, Geophys. Res. Lett., 37, L07105, doi:10.1029/2009GL042357.

Tsunoda, R. T. (2010b), On seeding equatorial spread F during solstices, Geophys. Res. Lett., 37, L05102, doi:10.1029/2010GL042576.

Tsunoda, R. T. (2010c), On seeding equatorial spread F: Circular gravity waves, Geophys. Res. Lett., 37, L10104, doi:10.1029/2010GL043422.

Valladares, C. E., Merriwether, J. W., Sheehan, R., and Biondi, M. A. (2002), Correlative study of neutral winds and scintillation drifts measured near the magnetic equator, J. Geophys. Res., 107(A7), doi:10.1029/2001JA000042.

Weber, E. J., Buchau, J., Eather, R. H., and Mende, S. B. (1978), North-south aligned equatorial airglow depletions, J. Geophys. Res., 83(A2), 712–716, doi:10.1029/JA083iA02p00712.

Whalen, J. A., Dependence of equatorial bubbles and bottomside spread F on season, magnetic activity, and E × B drift velocity during solar maximum, J. Geophys. Res., 107(A2), doi:10.1029/2001JA000039, 2002.

Whitney, H. E., and Malik, C. (1968). A proposed index for measuring ionospheric scintillation. Environmental Research Papers, 284, Technical Report, Airforce Cambridge Research Laboratories, United States.

Woodman, R. F., and La Hoz, C. (1976), Radar observations of F region equatorial irregularities, J. Geophys. Res., 81(31), 5447– 5466, doi:10.1029/JA081i031p05447.

Wright, C., Hindley, N., Alexander, M. J., Barlow, M., Hoffmann, L., Mitchell, C., Prata, F., Bouillon, M., Carstens, J., Clerbaux, C., Osprey, S., Powell, N., Randall, C., Yue, J., (2022), Tonga eruption triggered waves propagating globally from surface to edge of space, Earth and Space Science Open Archive, Retrieved from https://www.essoar.org/doi/abs/10.1002/essoar.10510674.1,doi:10.1002/essoar.10510674.1

Wright, R. W., J. R. Koster, N. J. Skinner (1956), Spread F-layer echoes and radio-star scintillation, *J. Atmos. and Terr. Phys.*, 8, 240-246, https://doi.org/10.1016/0021-9169(56)90129-5.

Wu, T.-W., Huba, J. D., Krall, J., Fritts, D. C., and Laughman, B. (2015), Seeding equatorial spread F with turbulent gravity waves: Phasing effects, Geophys. Res. Lett., 42, 15– 21, doi:10.1002/2014GL062348.

Yokoyama, T. (2017). A review on the numerical simulation of equatorial plasma bubbles toward scintillation evaluation and forecasting. Prog Earth Planet Sci 4, 37. https://doi.org/10.1186/s40645-017-0153-6.

Zettergren, M. D., Snively, J. B., Komjathy, A., and Verkhoglyadova, O. P. (2017), Nonlinear ionospheric responses to large-amplitude infrasonic-acoustic waves generated by undersea earthquakes, J. Geophys. Res. Space Physics, 122, 2272– 2291, doi:10.1002/2016JA023159.

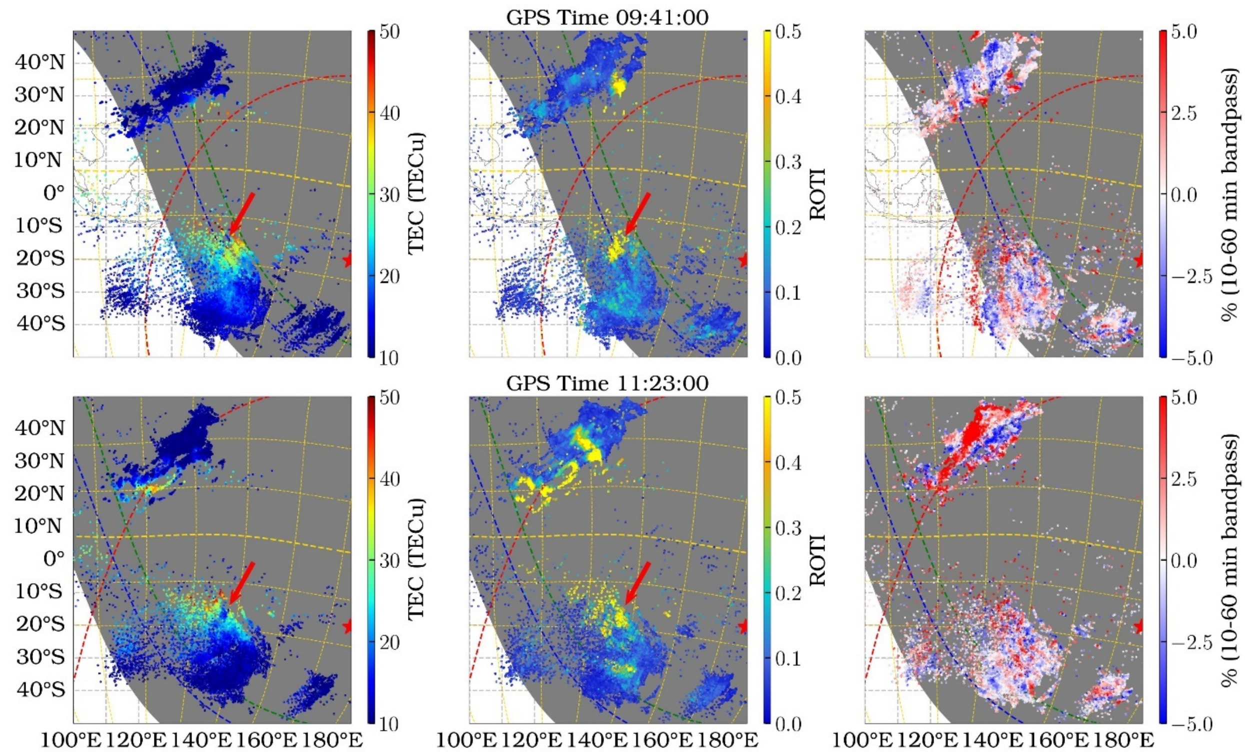

Figure 1. Ionospheric disturbances after the Tonga eruption. The (left) absolute TEC, (middle) ROTI, and (right) 10–60-minute band-pass filtered TEC with respect to the background are plotted at GPS times of (top) 0941 and (bottom) 1123 UT, respectively. The red arrow in the left panels indicate TEC depletions, where strong ROTI is also located. The red-dashed lines show the barometric Lamb wave (see Lin et al., 2022). The gray-shaded regions are under sunset with the blue- and green-dashed lines representing the E- and F-region terminators. The yellow grids give geomagnetic coordinates with thick dashed-line denoting magnetic equator.

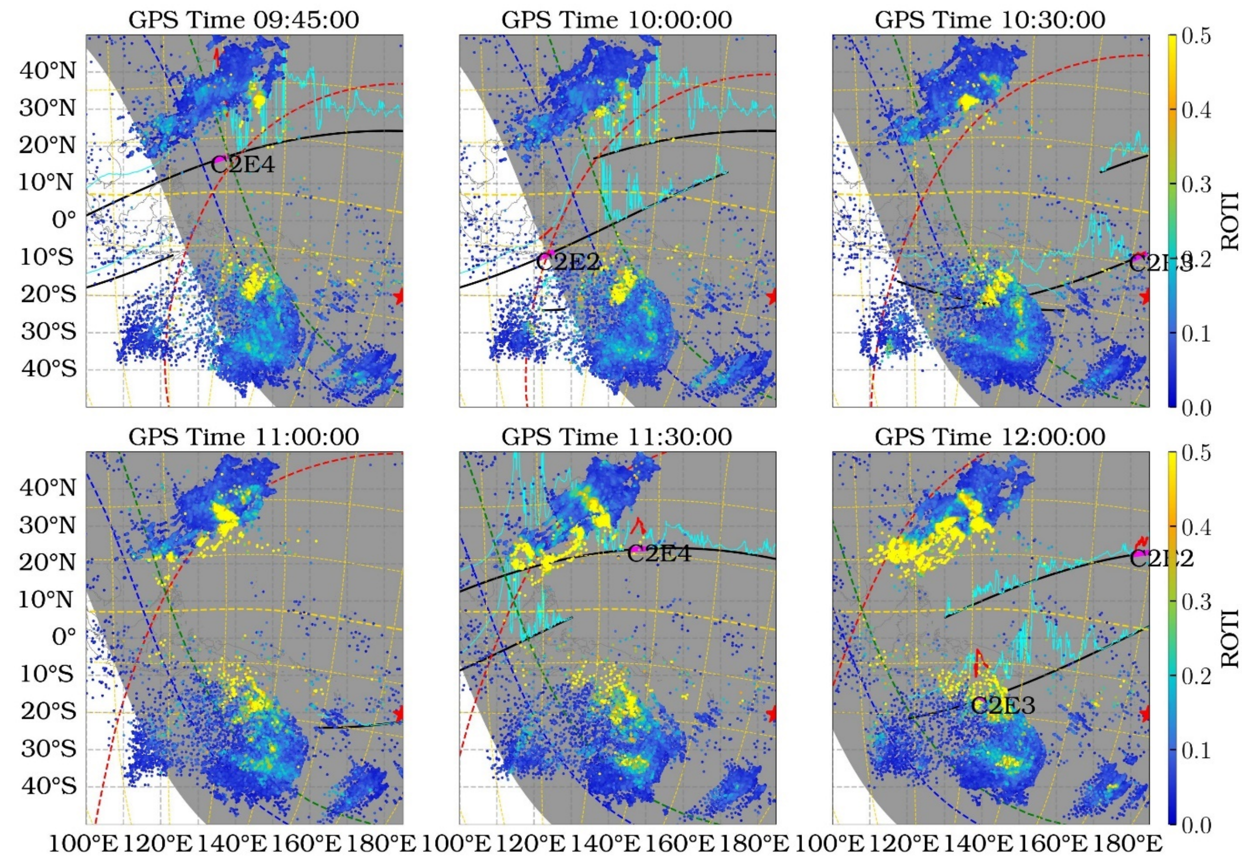

Figure 2. Similar to Figure 1, but only the ROTI maps at selected intervals, illustrating the poleward development of EPBs. Also plotted are the overpasses of F7/C2 during ±15 minutes (black lines), with the cyan lines showing IVM ion density measurements.

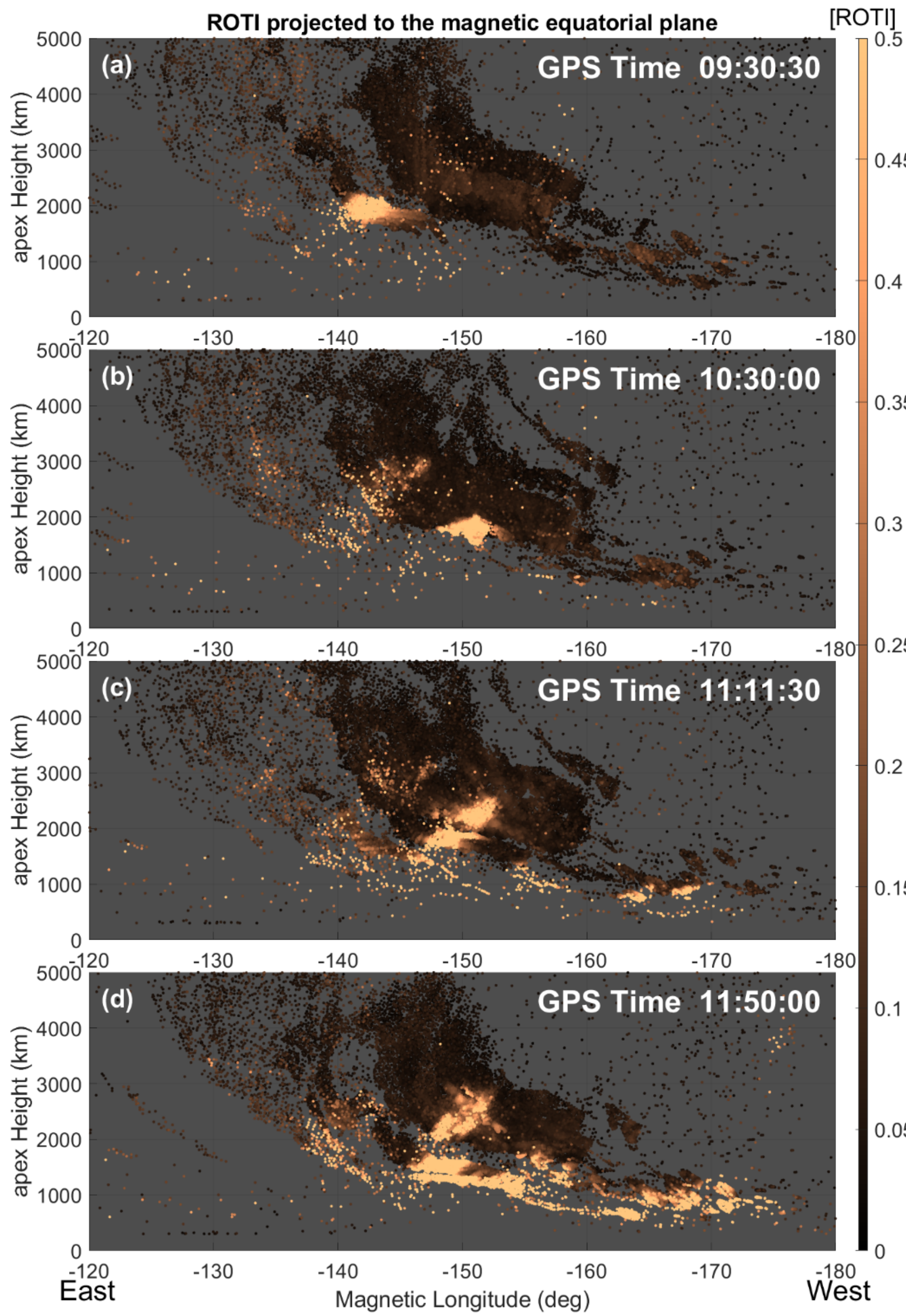

Figure 3. Apex altitude projection of the ROTI observations at selected intervals after the Tonga volcano eruption. The ROTI values in both the hemispheres are plotted together.

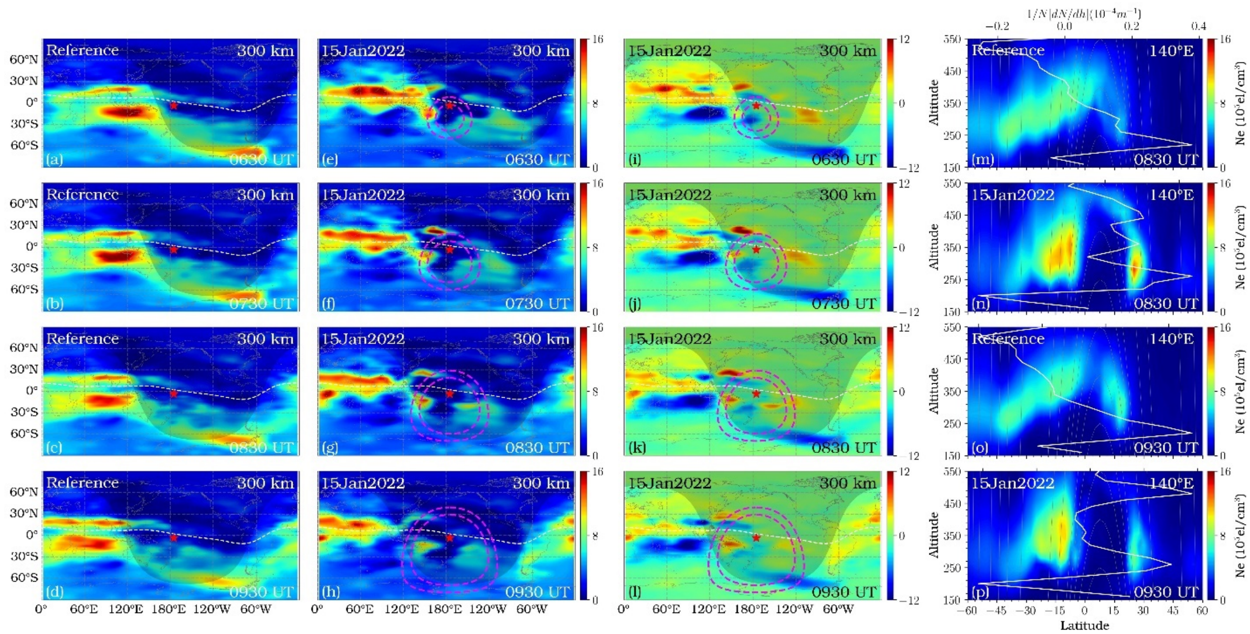

Figure 4. GIS electron density following the Tonga eruption. Panels (a)-(d) gives the reference latitude-longitude maps at 300 km during 0630-1030 UT, (e)-(h) on eruption day, and (i)-(l) gives the difference between the two. The latitude-altitude maps in panels (n) and (p) illustrate the intense PRE on 15 January compared to the reference day in (m) and (o). The white solid lines in (m)-(p) denote the altitude gradient of electron density, and the white dashed lines stand for the magnetic equator. The red-dashed curves in the second and third columns are the Lamb wave locations during the ±30 minutes period of the GIS assimilation, and the red asterisk denotes the location of Tonga. The shaded regions show longitudes after sunset.

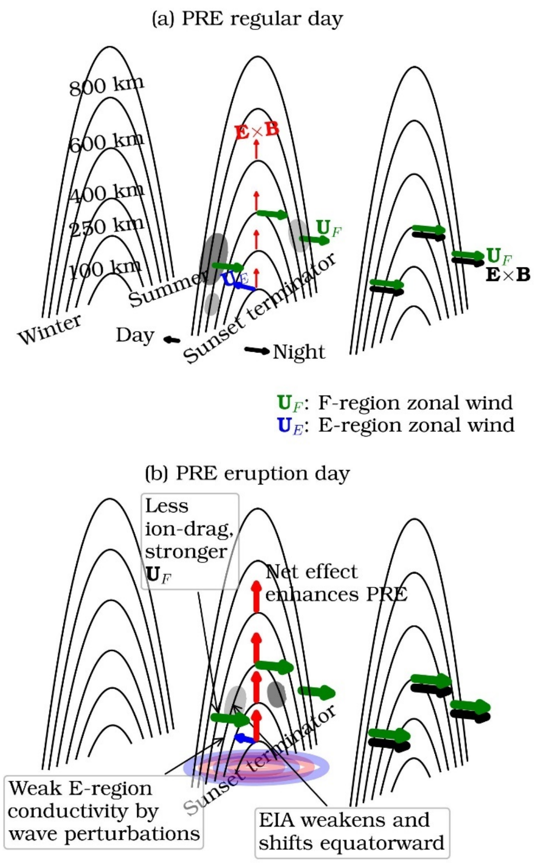

Figure 5. Sketch illustrating PRE. (a) On a regular day in solstice where finite E-region conductivity in southern hemisphere yields weak or no PRE. (b) After Tonga eruption during geomagnetic storm recovery. ExB drift by gravity waves (blue/red rings) decreases E-region conductivity in southern hemisphere, favoring PRE. Weakened EIA (gray-shaded area) by magnetic storm and eruption enable stronger $\mathbf{U}_F$, mobilizing ions and yielding upward vortical flow over the equator to supply more plasma, strengthening the PRE.

Geophysical Research Letters

Supporting Information for

Extreme poleward expanding super plasma bubbles triggered by Tonga volcano eruption during the recovery phase of geomagnetic storm

P. K. Rajesh[1], C. H. Charles Lin[1], J. T. Lin[1], C. Y. Lin[2,3], J. Y. Liu[2,3], T. Matsuo[4], C. Y. Huang[5], M. Y. Chou[6,7], J. Yue[6,7], M. Nishioka[8], H., Jin[8], J. M. Choi[1], S. P. Chen[1], Marty Chou[1], and H. F. Tsai[1]

[1] Department of Earth Sciences, National Cheng Kung University, Tainan, Taiwan

[2] Center for Astronautical Physics and Engineering, National Central University, Taoyuan, Taiwan

[3] Department of Space Science and Engineer, National Central University, Taoyuan, Taiwan

[4] Ann and H.J. Smead Department of Aerospace Engineering Sciences, University of Colorado Boulder, CO, USA

[5] National Space Organization, Hsinchu, Taiwan

[6] NASA Goddard Space Flight Center, Community Coordinated Modeling Center, Greenbelt,

MD, USA

[7] Physics Department, Catholic University of America, Washington, DC, USA

[8] The National Institute of Information and Communications Technology, Tokyo, Japan

Contents of this file

Figures S2 to S4

Additional Supporting Information (Files uploaded separately)

Captions for Movie S1

Introduction

Following the explosive eruption of the Tonga volcano, very intense plasma bubbles are observed over East Asian longitudes, revealing very strong ROTI values in the GNSS observations over Taiwan, Japan, Australia, and New Zealand, that expand to extreme poleward latitudes, reaching even beyond Tokyo. These ROTI observations, when projected to corresponding apex altitudes over the equatorial plain, offers a unique view of ROTI resembling vertically elongated radar plumes. Such apex projections at different time steps are used to extract the vertical rise velocity of the irregularities. The velocities are estimated separately for both the northern hemisphere and southern hemisphere observations, by noting the variation of uppermost the apex altitudes of the prominent ROTI regions at 140°E and 145°E longitudes seen in Movie S1. The calculated velocities are shown in Figure S2.

Prior to the generation of the plasma bubbles, very intense PRE was observed in the GIS electron density profiles. Such PRE is unusual in the solstice period under low solar activity. Figure S3 gives the time variation of the F-region peak altitude (hmF_2) and the peak density (nmF_2) at 140°E longitude on the day of the eruption, in comparison with the selected three reference days. The hmF_2 variation shows the strong PRE that lifted they layer by ~200 km for more than 3-hours. The time variation of hmF_2 is used to calculate the vertical rise velocity of F-layer, yielding ~40 m/s, compared to an average ~13 m/s based on the reference day measurements.

Figure S4 shows selected ionograms over Kokubunji in Japan and Townsville in Australia, showing the onset, and progression of spread-F on this day. Over Townsville, the ionograms appear to show the onset of range spread-F at the high-frequency end of the trace around 0914 UT (~1900 local time, LT), which later covers the entire transmitted frequencies in about 2-hours and manifests as complete spread-F by 1134 UT. The intense spread-F echoes that followed lasted the entire night (~0400 LT). The Kokubunji ionograms also reveal a similar progression with diffused high frequency traces from 1910 LT (1010 UT) but turn to complete spread-F by 2020 LT (1120 UT), lasting for several hours.

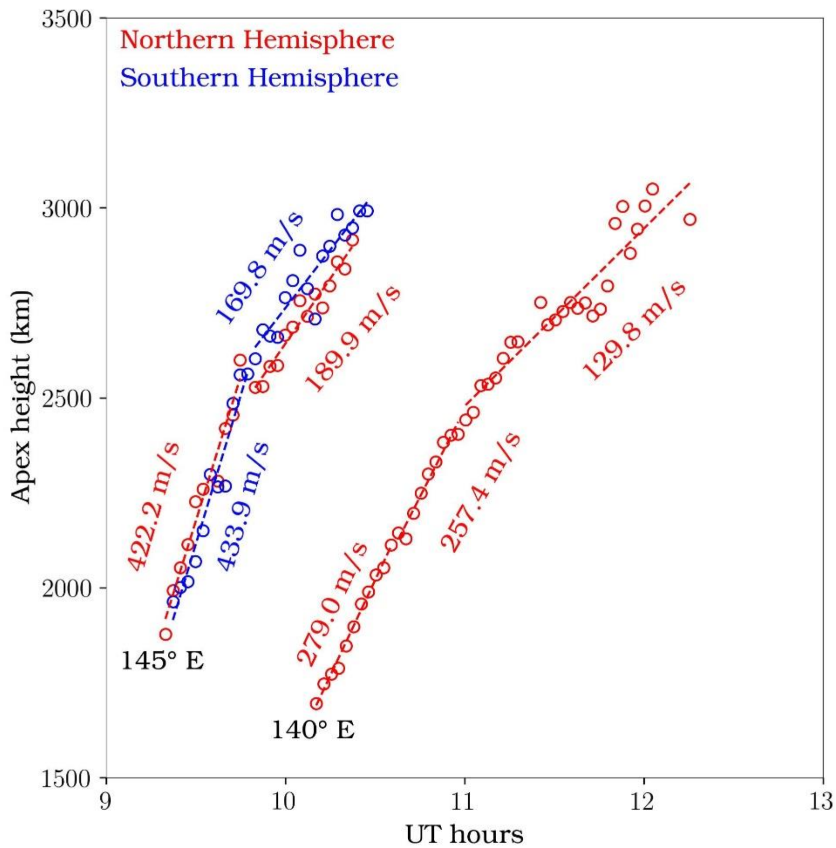

Figure S2. Vertical rise velocity of the palsma bubbles observed at 145° and 140°E, derived from Figure 3. The velocity is extracted by noting the variations of the apex altitudes of the selected ROTI regions at every 5-minute interval.

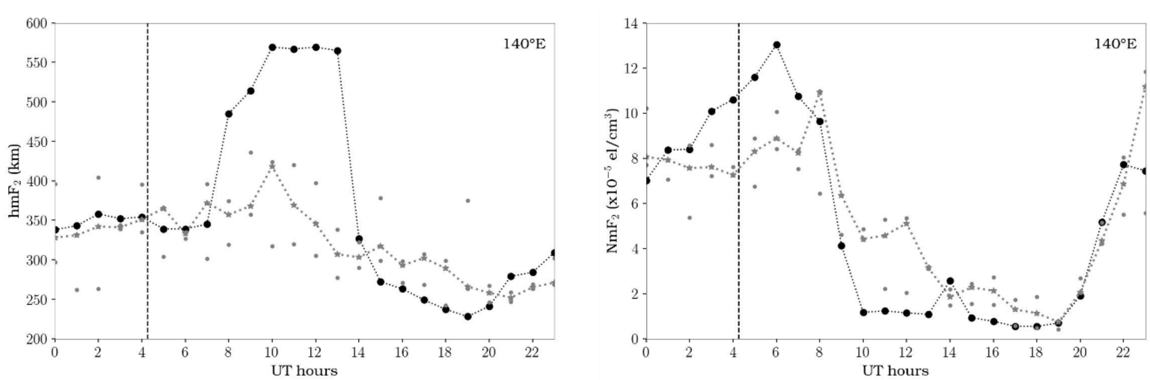

Figure S3. The hmF_2 and NmF_2 (black dots) on the eruption day derived from GIS electron density maps. The gray-line shows the median value of the previous quiet 3-day values (gray-dots). The vertical rise velocity estimated from the hmF_2 variation during 0700-1000 UT (1700-2000 LT) is ~40 m/s.

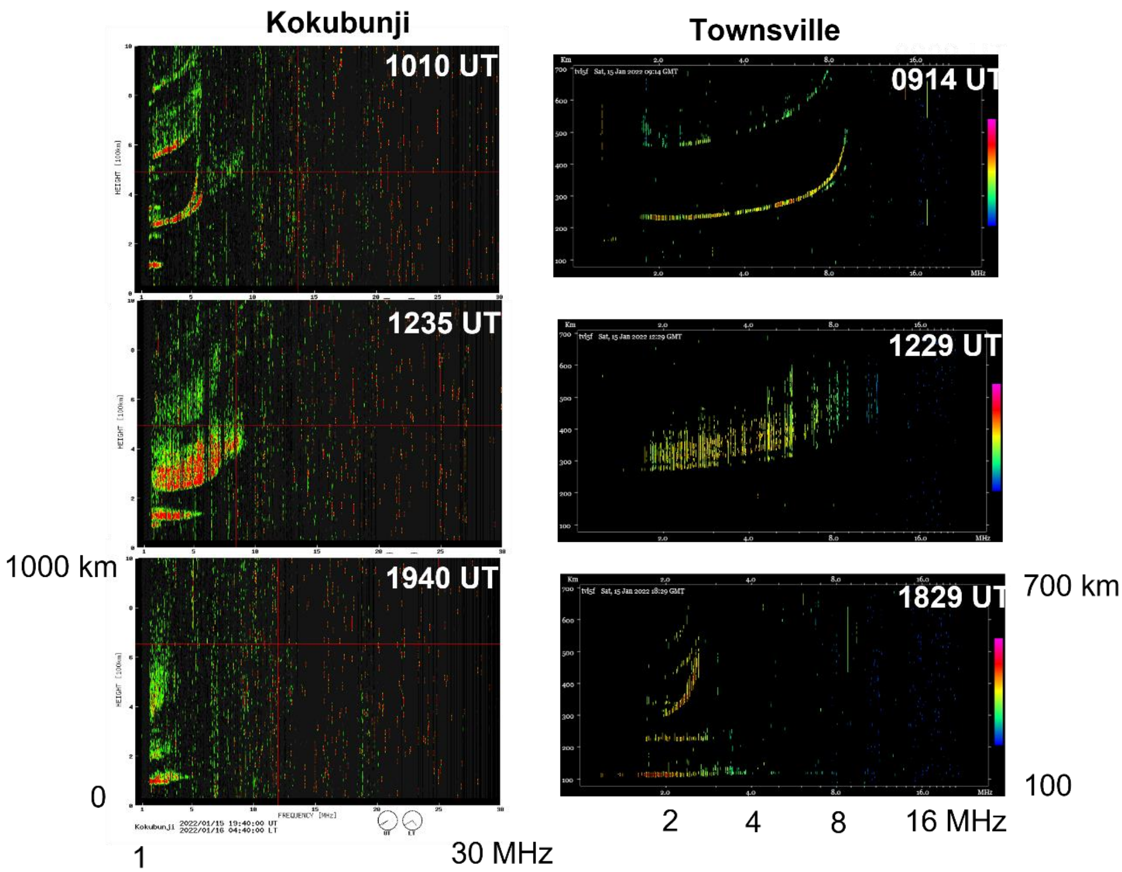

Figure S4. The Series of ionograms showing the (top) onset, (middle) peak and (bottom) end stage of spread-F at (left) Kokubunji and (right) Townsville.

Movie S1. A movie of the TEC, ROTI and filtered TEC values over the East Asian longitudes from 0400 hours to 1400 hours on 15 January 2022, illustrating the poleward expansion and eastward movements of strong ROTI locations. The format of the movie frames is same as that of the rows in Figure 1. The F7/C2 IVM observations at the corresponding time intervals are also overplotted on the ROTI maps, adopting the same format used in Figure 2.